Impact-Loss-Compensated Wideband Vibrational Energy Harvesting Using a Hybrid $BaTiO_3$/SU-8 Nanocomposite as the Active Layer

Nadeem Tariq Beigh, Sourav Naval, and Dhiman Mallick*
Department of Electrical Engineering, Indian Institute of Technology Delhi, New Delhi, India

(Received 5 July 2022; revised 17 September 2022; accepted 20 October 2022; published 18 November 2022)

Mechanical impact-induced nonlinearity proves to be effective in the tunable broadening of the frequency response in vibrational energy harvesters at various size scales. However, the substantial impact-induced power loss in impact-driven energy harvesters (IDEHs) negates such advantages. Here, an *in situ* power compensation mechanism is introduced to recover the impact-induced losses, and thereby, substantially enhance the energy harvesting efficiency. The proposed scheme is realized by designing an IDEH, where a dual transduction barium titanate/SU-8 based nanocomposite is used as the active layer. The piezoelectric transduction of the nanocomposite is used for conventional wideband power generation from the IDEH, whereas the additional triboelectric property enables the impact-induced loss compensation. The proposed improvement is quantified using a suitably defined figure-of-merit "power integral" (PI) that integrates the total power generated over the entire operational frequency range. The PI shows a shift from the region of impact loss to the region of compensation at input accelerations of < 1.5 g. Through suitable device engineering, the hybrid IDEH is experimentally shown to achieve 3.3 times power gain with bandwidth broadening of 5.4 Hz over conventional IDEH designs, which translates to 100% PI recovery. The underlying physics of the proposed method is independent of the device scale and is explained using a coupled numerical model.

DOI: 10.1103/PRXEnergy.1.033004

I. INTRODUCTION

Recently, energy harvesting from ambient sources has emerged as a viable solution for resolving the critical challenge of "powering a billion sensors" within the technological paradigm of the Internet of things [1]. Consequently, harvesting useful electrical power from ambient mechanical vibrations has attracted immense research interest due to their wide abundance in the majority of application scenarios, including wearable electronics, industrial monitoring, structural monitoring, and the automotive industry. [2]. Conventional vibrational energy harvesters (VEHs) are typically modeled as a second-order spring-mass-damper system, which provides maximum output power at resonance with a very narrow bandwidth, as defined by the Q factor of the system. A slight shift in the excitation frequency reduces the output power drastically. However, the majority of available ambient mechanical vibrations are either frequency varying (stationary or nonstationary) or wideband in nature. The so-called linear VEHs are not suitable to scavenge electrical energy from such sources efficiently. Several bandwidth broadening mechanisms are reported to overcome the "gain-bandwidth" dilemma, including multimode excitation [3,4]; resonance frequency tuning [5,6]; array-based harvester design [7,8]; and, most popularly, the introduction of controlled nonlinearity into the system dynamics for widening of the frequency response [9–11]. However, such wideband mechanisms usually require strict dimensional constraints, complex designs, and larger size implementation to augment an improved bandwidth. Resonance frequency tuning can be achieved using various mechanical and electrical techniques that are, however, not useful in most applications, as the energy required to implement tuning is often higher than the power harvested due to the added design complexity. On the other hand, multimode or array-based designs offer discrete frequency peaks with an increased device footprint, which reduces the power density significantly. By comparison, nonlinear oscillator based VEHs with monostable, bistable, or multistable potential wells can improve the off-resonance performance considerably [12]. Nonlinear spring structures with Duffing and higher-order polynomial restoring forces are adopted to widen the frequency response, as they can be suitably integrated onto various substrates [13–15]. However, they suffer from inherent hysteresis and multistability, which restrict their applications in real-life scenarios, especially under

*dhiman.mallick@ee.iitd.ac.in

random low-amplitude ambient excitation [16,17]. The snap-through (bistable or multistable) harvester design can potentially overcome such shortcomings but requires a significantly larger acceleration amplitude to initiate the large-amplitude interwell oscillations [18]. Moreover, conventional methods of introducing bistability require a repulsive magnetic interaction or prestressed beam design, which are either not scalable or hard to implement at the miniaturized scale [19].

On the other hand, VEHs with end stops produce a nonlinear impact force that results in a sudden drop in Q factor, leading to a flat wideband frequency response with a simple device design that can be customized at different size scales [20,21]. Recently, impact-driven energy harvesters (IDEHs) have reported 200% increase in frequency bandwidth [22]. However, such significant bandwidth improvement due to the piecewise linear frequency response is attained at the cost of reduced output power. The impact-induced power loss is substantial, and the overall efficiency is lower than that of the non-impact-driven VEHs [23,24]. Thus, impact due to the stoppers can lead to insufficient energy transduction where a considerable impact-induced power loss negates the widened bandwidth. Such designs are, however, compelling, as they do not suffer from any hysteresis or require a special arrangement for the bandwidth widening mechanism. Hence, it will be really beneficial to use the end stoppers, as part of the harvester structure, as an additional energy generation component rather than just a loss-inducing mechanism.

Here, we aim to address the abovementioned challenges by designing a highly efficient IDEH where a hybrid BTO/SU-8 based nanocomposite is used for dual-energy transduction, facilitating a unique energy compensation route via its piezoelectric and triboelectric properties to overcome the impact loss that affects the net energy harvesting efficiency. Section II introduces the impact-loss compensation mechanism supported suitably with a detailed material characterization. Section III presents a detailed theoretical framework of the proposed piezoelectric and triboelectric hybrid IDEH (HIDEH). Finally, in Sec. IV, we analyze the experimental parametric study to delineate different operational regimes by a suitably defined figure-of-merit of "power integral" (PI).

II. IMPACT-LOSS COMPENSATION MECHANISM

The concept of the dual transduction nanocomposite-based VEH is illustrated in Fig. 1. It depicts the output power of a VEH as a function of the operational frequency for a linear piezoelectric energy harvester (LPEH) [25], piezoelectric IDEH (PIDEH) [26], compensating triboelectric energy harvester (CTEH) [27], and the combined HIDEH. The LPEH exhibits a characteristic narrowband response, wherein the cantilever free-end displacement is constrained within the initial gap between the beam and

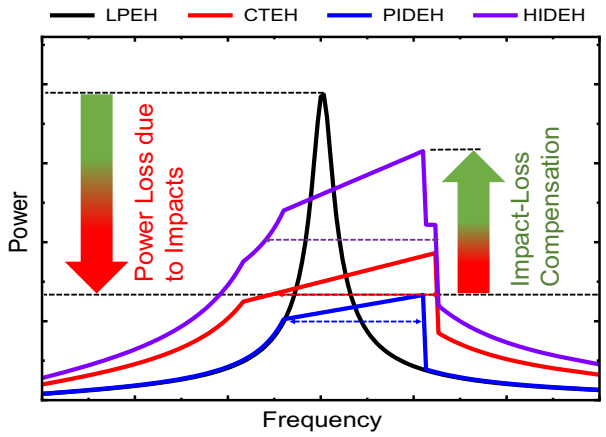

FIG. 1. Illustration of the principle of impact-energy-loss compensation using the proposed HIDEH.

stopper. As evident from Fig. 1, the peak power decreases significantly for a PIDEH, owing to the impact-induced power loss. On the other hand, impact induces contact between the triboelectric layers (nanocomposite and stopper) in the case of the CTEH. The impact-induced contact and the relative separation (approach) between the contacting layers is fundamental for producing the triboelectric output. Hence, the CTEH output response is significantly larger for the given frequency range. Combining the PIDEH and CTEH results in the HIDEH response, which inherits a large output and a wider bandwidth. The proposed design recovers the impact-induced loss by substituting the existing impact-loss-generation mechanisms (stoppers) with a impact-loss-compensation mechanism (stopper with dual transduction nanocomposite).

The BTO/SU-8-based HIDEH is fabricated on an ITO-coated polyethylene terephthalate (PET) sheet substrate. Figure 2(a) shows the device schematic and identifies all the layers. An optimized 20% weight ratio BTO/SU-8 nanocomposite thin film is developed using the detailed fabrication steps given in Fig. S1 within the Supplemental Material [39]. The combination of highly piezoelectric BTO nanoparticles embedded within the SU-8 matrix [Fig. 2(c)] produces a high-performance nanocomposite with high compliance, uniform strain distribution, and improved sustainability. The piezoelectric properties of the BTO/SU-8 nanocomposite were extensively studied in our previous work [28]. However, such nanocomposites also show triboelectric behavior due to the polymeric nature of the SU-8 base matrix [29]. The developed BTO/SU-8 nanocomposite is attractive in terms of ease of preparation, low-temperature processing, photopatternability for large-scale fabrication, etc. Additionally, by combining piezoelectric and triboelectric transductions into a single thin film, the BTO/SU-8 nanocomposite avoids the requirement for additional fabrication steps. Elaborate details about the piezoresponse

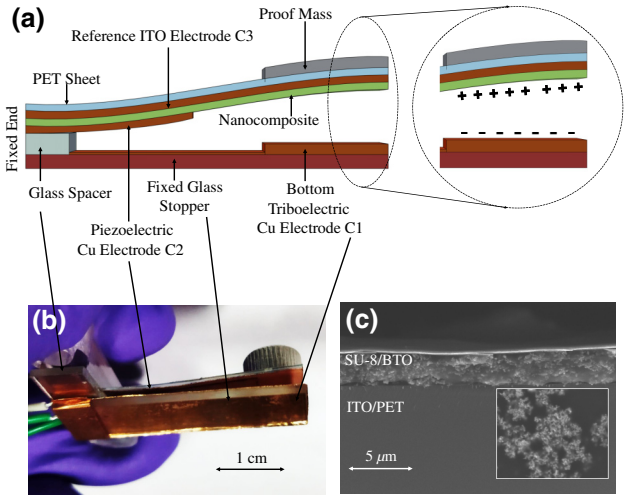

FIG. 2. (a) Schematic of the proposed device. Inset shows the relative charge distribution between nanocomposite and triboelectric electrodes. (b) As-fabricated device prototype. (c) SEM image of the optimized nanocomposite.

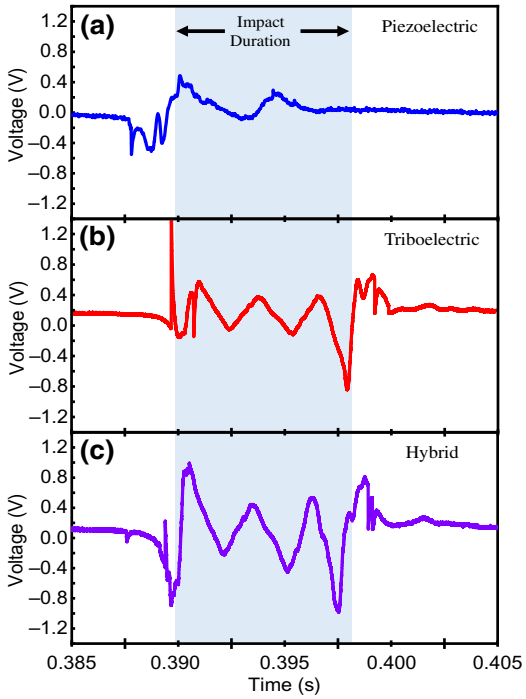

FIG. 3. Time responses of (a) piezoelectric, (b) triboelectric, and (c) hybrid outputs of the HIDEH device at 1-g input acceleration.

force microscopy, kelvin probe force microscopy (KPFM), x-ray diffraction, and scanning electron microscopy (SEM) measurements are given in the Supplemental Material [39] to further support the claim of the dual piezoelectric and triboelectric properties of the % weight ratio optimized nanocomposite. The fabricated device prototype, shown in Fig. 2(b), has a footprint of 3×1 cm^2 on a 150-μm substrate with nanocomposite thickness of 6.5 μm. An additional proof mass of 1.2 g is epoxy bonded to bring the working frequency of the device below 50 Hz. A partially covered copper tape on top of the nanocomposite with dimensions of 1 cm $\times$ 1 cm $\times$ 150 μm forms piezoelectric electrode C2. The copper triboelectric electrode C1 (3 cm $\times$ 1 cm $\times$ 150 μm) covers the entire 1-mm-thick glass stopper, while the underlying ITO layer on the PET substrate acts a common ground electrode, C3.

This paper focuses on high acceleration amplitude vibrations that initiate the impact of the cantilever beam with the stiff triboelectric electrode. The piezoelectric and triboelectric responses of the device are measured using a closed loop controlled electrodynamic shaker, as shown in Fig. S8 within the Supplemental Material [39]. The output terminals, triboelectric (C1–C3) and piezoelectric (C2–C3), are connected to two channels of a digital oscilloscope (PicoScope 3000 series) using load resistances of 10 and 100 MΩ, respectively. Piezoelectric, triboelectric, or both effects co-occur, depending on the acceleration amplitude, and thereby, divide the operation into pre- and postimpact regions. Upon contact between the Cu electrode and the nanocomposite film, electrical charge is transferred as a consequence of the large difference in work functions [30,31]. This transfer induces the opposite charge on the other side of the nanocomposite thin film, resulting in a net triboelectric current pulse (I_{tr}) between C1 and C3. Furthermore, the deformation-induced strain in the nanocomposite produces piezoelectric polarization that results in a piezoelectric current (I_{PZ}) between C2 and C3. The hybrid output accumulates both responses and is acquired by shorting C2–C3 and measuring the output with respect to C1. The sign of I_{PZ} is determined by the direction of effective polarization of the nanocomposite. Therefore, the hybrid current, I_{hyb}, is either suppressed, $I_{hyb} = I_{tr} - I_{PZ}$, or enhanced, $I_{hyb} = I_{tr} + I_{PZ}$, depending on the value of I_{PZ}. Figure 3 is shown to clarify the difference between piezoelectric, triboelectric, and hybrid responses during the impact duration at 1-g acceleration and at a frequency of 50 Hz. The piezoelectric response [Fig. 3(a)] damps down after the impact, while the triboelectric response becomes more prominent during the impact (contact) between the electrode and the nanocomposite. The physical impact between contacting layers results in the induction of maximum strain in the piezoelectric layer; hence, the sudden peak in the response is observed [24]. Meanwhile, the impact triggers contact between the nanocomposite layer and the stiff triboelectric electrode, resulting in complete charge neutralization, which appears as a voltage spike across the load resistor. The hybrid output combines both responses and provides a larger output compared to the stand-alone piezoelectric response, which, however, depends on the phase difference between different responses.

III. THEORETICAL FRAMEWORK

Both triboelectric and piezoelectric transduction mechanisms of the developed IDEH can be represented by the simplified capacitive models given in Eqs. (1)–(3), (6), and (7). For triboelectric modeling, the electric field across the nanocomposite and air is given by Eq. (1) [32,33].

$$E_{\mathrm{NC}} = \frac{q(t)}{\epsilon_O \epsilon_{\mathrm{NC}} A} \text{ and } E_{\mathrm{air}} = \frac{\frac{q(t)}{A} + \sigma}{\epsilon_O} \tag{1}$$

$$v(t)_{\mathrm{tr}} = i(t)_{\mathrm{tr}} R_t = R_t \dot{q}(t) = E_{\mathrm{NC}}\delta + E_{\mathrm{air}}(\Delta - z) \tag{2}$$

$$F_e = \frac{\epsilon_0 \epsilon_{\mathrm{NC}} A (v_{\mathrm{tr}}(t))^2}{2z^2} = \frac{q(t)^2}{2\epsilon_O \epsilon_{\mathrm{NC}} A} \tag{3}$$

$$m_{\mathrm{eff}}\ddot{z} + c_b\dot{z} + k_{\mathrm{eff}} z + \theta v - q^2/(2\epsilon_o \epsilon_{\mathrm{NC}} A) = m_{\mathrm{eff}}\, a\, \sin\omega t \quad \forall\, z(t) < \Delta \tag{4}$$

$$m_{\mathrm{eff}}\ddot{z} + (c_b + c_i)\dot{z} + k_{\mathrm{eff}} z + K_{\mathrm{imp}}(z - \Delta) + \theta v = m_{\mathrm{eff}}\, a\, \sin\omega t \quad \forall\, z(t) \geq \Delta \tag{5}$$

$$R_t \frac{\partial q}{\partial t} = -\frac{q}{A\epsilon_o}\left(\frac{\delta}{\epsilon_{\mathrm{NC}}} + \Delta - z\right) + \frac{\sigma(\Delta - z)}{\epsilon_o} \tag{6}$$

$$C_p \dot{v} + \frac{v}{R_p} = \theta \dot{z} \tag{7}$$

The triboelectric voltage induced across the electrodes is contributed to by the electric field components of the nanocomposite and air. Hence, the instantaneous triboelectric voltage, v_{tr}, is given by Eq. (2). Here, E_{NC}, E_{air}, $q(t)$, σ, A, ϵ_{NC}, ϵ_{air}, R_t, δ, Δ, and z are the electric field across the nanocomposite, the electric field across air, the instantaneous triboelectric charge, the surface charge density on contacting materials, the effective area of contact, the effective permittivity of the nanocomposite, the permittivity of air, the load resistance for triboelectric output, the thickness of the nanocomposite, the initial gap between contacting layers, and the cantilever free-end displacement. The dual-energy scavenging system can be represented by a set of coupled differential equations, Eqs. (4)–(7). The electrostatic force, F_e, developed between the contacting materials is given by Eq. (3) and appears as an additional excitation in the equation of motion of the impacting cantilever [Eq. (4)] [24,34], where m_{eff}, c_b, k_{eff}, θ, a, c_i, k_{imp}, C_p, v, and R_p are the effective cantilever mass, the damping ratio, the effective linear stiffness of the cantilever, the piezoelectric coupling coefficient, the external acceleration amplitude, the damping ratio for the impacting electrode, the effective stiffness of the impact electrode, the piezoelectric capacitance of the nanocomposite, the piezoelectric output voltage, and the load resistance for piezoelectric output. Equations (4) and (5) represent the pre- and postimpact equations of motion of the piezoelectric cantilever. Equation (6) represents the instantaneous triboelectric voltage equation coupled to Eq. (4) via the cantilever free-end displacement, z. The last term of Eq. (6) is the open-circuit voltage (v_{OC}) and is related to the work function of triboelectric layers as $\sigma(\Delta - z)/\epsilon_o = C_p(\phi_{\mathrm{film}} - \phi_{\mathrm{elec}})(z(t)/eA\epsilon_o)$ [35]. Equation (7) is the general piezoelectric coupled equation for a cantilever resonator with $\theta\dot{z}$ is the coupling term with Eqs. (4) and (5).

IV. RESULTS AND DISCUSSION

A. Parametric study of impact-loss compensation

The correlation of operational bandwidth, harvested power, and power loss with acceleration amplitude are computed from the developed analytical model using the simulation parameters given in Table S1 within the Supplemental Material [39]. The simulation parameters are chosen based on the application frequency range, acceleration amplitude, piezoelectric and triboelectric material properties, etc. The complete details of the simulation parameters are given in the Supplemental Material [39]. Figure 4(a) illustrates the simulated dependence of the same for LPEH and PIDEH. Initially, the bandwidth and peak power for both types of operation show exactly the same variation, as expected. After the onset of impact (at 0.3 g in this case), the bandwidth for the conventional PIDEH increases sharply, whereas the peak power almost saturates. The corresponding variations for the LPEH are further shown by the dotted lines. In the case of the PIDEH, the cantilever free-end displacement is restricted by the fixed stopper that ensues from mechanical impact, and the piecewise linear nature is augmented at higher accelerations, which expand the bandwidth considerably. However, the rate of change of peak power reduces sharply from 10.4 μW/g in LPEH to 1.29 μW/g in PIDEH at 1 g. This significant change in bandwidth and power for pre- and postimpact operations is a direct consequence of the impact. The trade-off between bandwidth, output power, and impact-power loss indicate the necessity for an impact-loss compensating mechanism in the design of the PIDEH to operate efficiently.

The comparative experimental frequency responses under different operating conditions of the device are given in Fig. 4(b) for 1-g acceleration and a frequency range of 30–70 Hz. The conventional PIDEH generates a peak power of 1 μW at 50.1 Hz, which is 7 μW lower than the same for the LPEH (resonance frequency = 43.9 Hz), whereas the bandwidth increases by 7 Hz. Incorporating the CTEH in the design provides a 3 times higher peak power at 56.3 Hz with slight broadening of the bandwidth, as compared to the PIDEH. The unification of the PIDEH and CTEH results in a HIDEH response, contributing an additional increment of 3 μW in the peak power and bandwidth broadening of 5.4 Hz over the PIDEH. The peak power in the HIDEH is only 5 μW lower than the LPEH. As illustrated in Fig. 4(b), the generated hybrid response is significantly larger in amplitude and bandwidth than that of the PIDEH, since the combined transduction produces $I_{\mathrm{hyb}} = I_{\mathrm{tr}} \pm I_{\mathrm{PZ}}$ over the given frequency range.

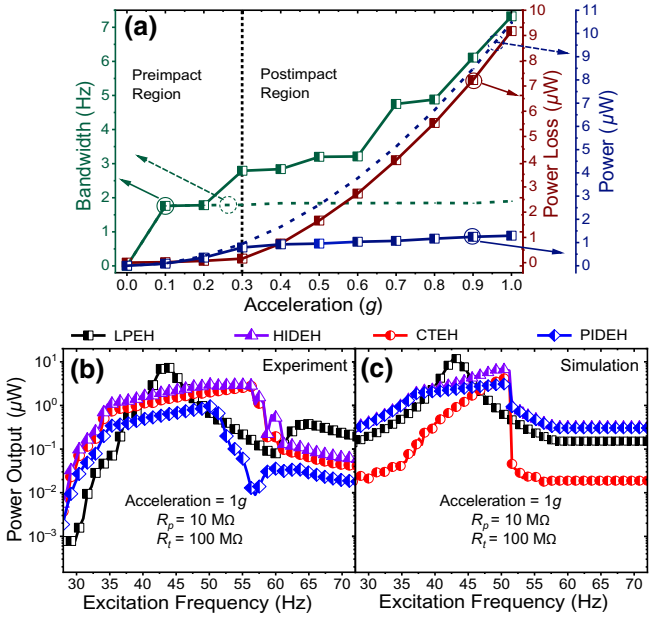

FIG. 4. (a) Bandwidth, peak power, and power-loss dependence on acceleration for PIDEH (solid lines) and LPEH (dotted lines), depicting pre- and postimpact regions. Frequency responses for different VEH operations at 1 g: (b) Experimental (c) Simulation.

The enhanced output response of the HIDEH signifies that the additional power generated can overcome the inherent impact-induced loss in the PIDEH. The experimental results are further validated by numerically solving the analytical model of the HIDEH using the ode23s solver. Simulated responses are given in Fig. 4(c), which match well with the experimental results. However, slight deviations are observed due to unavoidable material and geometric damping in the contacting layers of the device and cantilever clamping. Moreover, the influence of the surface roughness and increased contact area on CTEH output is not incorporated in the numerical model to avoid computational complexities.

B. Power integral analysis

To effectively compare the usefulness of the proposed method, a suitably defined figure-of-merit PI is used [36,37]. The PI is defined as the area under the output power-frequency curve at a fixed acceleration and is given by $Þ = \int (P\partial f)$, where P is the output power across the load. This figure of merit quantifies the performance of an energy harvester by considering both output power and bandwidth together [Fig. S5(a) within the Supplemental Material [39]]. The PI values are calculated experimentally for each operating condition over a frequency range of 30–70 Hz and input accelerations of $0 - 2.0$ g. $Þ_{CTEH}$, $Þ_{PIDEH}$, and $Þ_{LPEH}$ refer to the PI values of the compensating TEH, PIDEH, and LPEH outputs. A differential parameter, $\Delta Þ = Þ_{CTEH} + Þ_{PIDEH} - Þ_{LPEH}$, is an indicator of the energy-loss compensation at different acceleration amplitudes. A positive value of $\Delta Þ$ symbolizes energy compensation, as the combined PI value of $Þ_{CTEH} + Þ_{PIDEH}$ becomes greater than $Þ_{LPEH}$. The experimentally obtained PI values as a function of acceleration are shown in Fig. 5(a). The difference in $Þ_{CTEH} + Þ_{PIDEH}$ and $Þ_{LPEH}$ increases further as the acceleration amplitude becomes greater than 1 g and can be attributed to a larger impact force, increased triboelectric contact area, larger strain, and increase in the surface charge density of the nanocomposite [38]. For lower accelerations, $Þ_{CTEH}$ is negligible due to either no or minimal impact but increases beyond 0.3 g. The rapid rise in $Þ_{CTEH}$ indicates complete impact and triboelectrification, which improves further for higher accelerations due to the aforementioned reasons. $Þ_{PIDEH}$ follows $Þ_{LPEH}$ for lower accelerations, as both parameters should ideally be the same during preimpact operation. The reduction in $Þ_{PIDEH}$ in postimpact operation is noticeable [Fig. 5(a)] and is associated with the impact-induced power loss. For higher accelerations, $Þ_{PIDEH}$ shows a modest improvement, owing to the improved bandwidth but at the cost of significant power loss. The simulated acceleration dependence of the PI shown in Fig. 5(b) is in good agreement with the experimental results. In both results, the PI compensation occurs beyond 1-g acceleration amplitude as the cantilever free-end displacement becomes greater than the initial gap (of 1 mm), and triboelectric transduction comes into the picture. This increase in $\Delta Þ$ causes a transition from a negative to a positive value [Figs. S5(b) and S5(c) within the Supplemental Material [39]], namely, from the ROIL to the ROC. As $Þ_{PIDEH}$ and $Þ_{LPEH}$ increase linearly with the acceleration amplitude, the PI gain is mainly due to the additional triboelectric transduction of the BTO/SU-8 nanocomposite. The impact-loss-compensation mechanism completely recovers the PI loss of 50 μW Hz in PIDEH and gives an additional PI gain of 63 μW Hz for acceleration lower than 1.5 g. Alternatively, a normalized power integral density (NPID), given by Eq. (8), is defined along with the PI, to provide a better comparison between the operational regions of the proposed device.

$$\eta = \frac{Þ}{\text{volume}} \tag{8}$$

The η values for $Þ_{PIDEH}$, $Þ_{LPEH}$, $Þ_{CTEH}$, and $\Delta Þ$ are 34.2, 100, 111, and 45 W Hz m^{-3}, respectively, for acceleration lower than 1.5 g. A positive η value for $\Delta Þ$ provides further confirmation of impact-energy-loss compensation in the proposed design. Therefore, incorporating the BTO/SU-8 nanocomposite as an active layer in the PIDEH is advantageous and supports the initial claim of impact-energy-loss compensation. Henceforth, the dual transduction of the BTO/SU-8 nanocomposite in an IDEH can obtain a large PI value, signifying a high output power and bandwidth compared to conventional IDEHs.

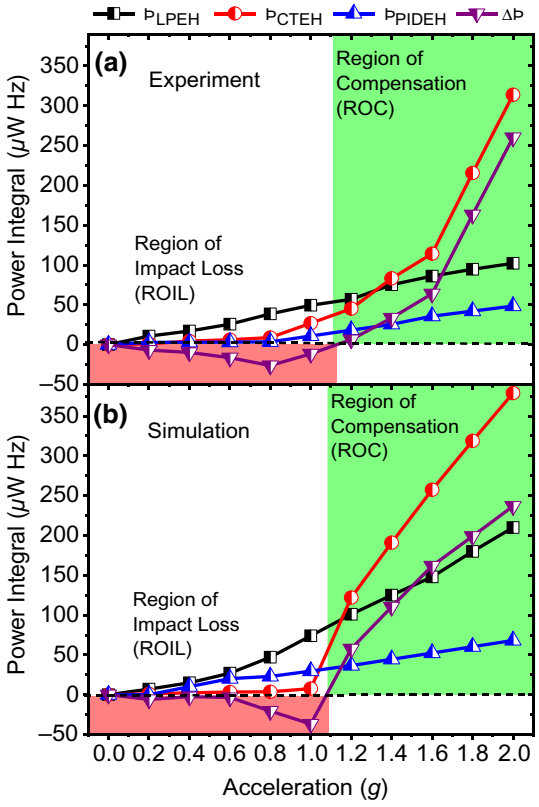

FIG. 5. PI versus acceleration illustrating the region of impact loss (ROIL) and region of compensation (ROC) for different operational regions: (a) experiment and (b) simulation.

V. CONCLUSION

A hybrid transduction IDEH is presented with an inherent impact-power-loss compensation mechanism. The presented IDEH is capable of compensating for impact-induced energy loss by 100% PI recovery at < 1.5-g acceleration amplitude. Such significant enhancement in the energy harvesting performance is achieved by suitably designing a device that incorporates a dual piezoelectric and triboelectric transduction-based nanocomposite as the active layer. The HIDEH demonstrates 3.3 times power gain and a bandwidth broadening of 5.4 Hz at (1 g) that translates to full PI recovery of 50 μW Hz in the conventional PIDEH. The reported design with dual transduction is highly scalable and overcomes the typical gain-bandwidth dilemma of nonlinear wideband IDEHs, thereby further diversifying their applications in various energy harvesting and inertial sensing applications.

Data supporting this study's findings are available within the article and in the Supplemental Material [39].

ACKNOWLEDGMENTS

This work is supported by the I-HUB Foundation for Cobotics, IIT Delhi (Project No. RP04218G). The authors would also like to thank CARE, NRF, and CRF at IIT Delhi for providing the experimental facilities and thank Ms. Shalini Singh and Professor Ankur Goswami of DMSE, IIT Delhi, for helping with the AFM and KPFM measurements.

[1] T. Becker, V. Borjesson, O. Cetinkaya, C. Baoxing, J. Colomer-Farrarons, D. Maeve, A. Elefsiniotis, L. Govoni, Z. Hadas, M. Hayes *et al.*, in *PSMA White Paper Series* (PSMA, 2021), p. 1.

[2] M. Shirvanimoghaddam, K. Shirvanimoghaddam, M. M. Abolhasani, M. Farhangi, V. Z. Barsari, H. Liu, M. Dohler, and M. Naebe, Towards a green and self-powered internet of things using piezoelectric energy harvesting, IEEE Access **7**, 94533 (2019).

[3] D. Liu, H. Li, H. Feng, T. Yalkun, and M. R. Hajj, A multi-frequency piezoelectric vibration energy harvester with liquid filled container as the proof mass, Appl. Phys. Lett. **114**, 213902 (2019).

[4] D. Mallick, P. Constantinou, P. Podder, and S. Roy, Multi-frequency MEMS electromagnetic energy harvesting, Sens. Actuators, A **264**, 247 (2017).

[5] L. Gu and C. Livermore, Passive self-tuning energy harvester for extracting energy from rotational motion, Appl. Phys. Lett. **97**, 081904 (2010).

[6] D. Mallick and S. Roy, Bidirectional electrical tuning of FR4 based electromagnetic energy harvesters, Sens. Actuators, A. **226**, 154 (2015).

[7] I. Abed, N. Kacem, N. Bouhaddi, and M. L. Bouazizi, Multi-modal vibration energy harvesting approach based on nonlinear oscillator arrays under magnetic levitation, Smart Mater. Struct. **25**, 025018 (2016).

[8] D. Upadrashta and Y. Yang, Nonlinear piezomagnetoelastic harvester array for broadband energy harvesting, J. Appl. Phys. **120**, 054504 (2016).

[9] L. Gammaitoni, I. Neri, and H. Vocca, Nonlinear oscillators for vibration energy harvesting, Appl. Phys. Lett. **94**, 164102 (2009).

[10] B. Marinkovic and H. Koser, Smart sand–a wide bandwidth vibration energy harvesting platform, Appl. Phys. Lett. **94**, 103505 (2009).

[11] W. Wang, J. Cao, C. R. Bowen, D. J. Inman, and J. Lin, Performance enhancement of nonlinear asymmetric bistable energy harvesting from harmonic, random and human motion excitations, Appl. Phys. Lett. **112**, 213903 (2018).

[12] R. L. Harne and K. Wang, A review of the recent research on vibration energy harvesting via bistable systems, Smart Mater. Struct. **22**, 023001 (2013).

[13] X. Dai, X. Miao, L. Sui, H. Zhou, X. Zhao, and G. Ding, Tuning of nonlinear vibration via topology variation and its application in energy harvesting, Appl. Phys. Lett. **100**, 031902 (2012).

[14] G. Gafforelli, A. Corigliano, R. Xu, and S.-G. Kim, Experimental verification of a bridge-shaped, nonlinear vibration energy harvester, Appl. Phys. Lett. **105**, 203901 (2014).

[15] D. Mallick, A. Amann, and S. Roy, A nonlinear stretching based electromagnetic energy harvester on FR4 for wideband operation, Smart. Mater. Struct. **24**, 015013 (2014).

[16] Y. Zhang, R. Zheng, K. Nakano, and M. P. Cartmell, Stabilising high energy orbit oscillations by the utilisation of centrifugal effects for rotating-tyre-induced energy harvesting, Appl. Phys. Lett. **112**, 143901 (2018).
[17] D. Mallick, A. Amann, and S. Roy, Surfing the High Energy Output Branch of Nonlinear Energy Harvesters, Phys. Rev. Lett. **117**, 197701 (2016).
[18] R. Xu, H. Akay, and S.-G. Kim, Buckled MEMS beams for energy harvesting from low frequency vibrations, Research **2019**, 1 (2019).
[19] Y. Jia, Review of nonlinear vibration energy harvesting: Duffing, bistability, parametric, stochastic and others, J. Intel. Mater. Syst. Struct. **31**, 921 (2020).
[20] S. C. Stanton, C. C. McGehee, and B. P. Mann, Reversible hysteresis for broadband magnetopiezoelastic energy harvesting, Appl. Phys. Lett. **95**, 174103 (2009).
[21] Y. Lu, F. Cottone, S. Boisseau, F. Marty, D. Galayko, and P. Basset, A nonlinear MEMS electrostatic kinetic energy harvester for human-powered biomedical devices, Appl. Phys. Lett. **107**, 253902 (2015).
[22] M. Song, Y. Zhang, M. Peng, and J. Zhai, Low frequency wideband nano generators for energy harvesting from natural environment, Nano Energy **6**, 66 (2014).
[23] H. Liu, C. J. Tay, C. Quan, T. Kobayashi, and C. Lee, A scrape-through piezoelectric MEMS energy harvester with frequency broadband and up-conversion behaviors, Microsyst. Technol. **17**, 1747 (2011).
[24] P. Thainiramit, P. Yingyong, and D. Isarakorn, Impact-driven energy harvesting: Piezoelectric versus triboelectric energy harvesters, Sensors **20**, 5828 (2020).
[25] A. Erturk and D. J. Inman, On mechanical modeling of cantilevered piezoelectric vibration energy harvesters, J. Intell. Mater. Syst Struct. **19**, 1311 (2008).
[26] E. Jacquelin, S. Adhikari, and M. I. Friswell, A piezoelectric device for impact energy harvesting, Smart. Mater. Struct. **20**, 105008 (2011).
[27] C. Zhao, Y. Yang, D. Upadrashta, and L. Zhao, Design, modeling and experimental validation of a low-frequency cantilever triboelectric energy harvester, Energy **214**, 118885 (2021).
[28] N. T. Beigh and D. Mallick, Low-cost, high-performance piezoelectric nanocomposite for mechanical energy harvesting, IEEE Sens. J. **21**, 21268 (2021).
[29] N. T. Beigh, S. Singh, A. Goswami, and D. Mallick, Dual piezoelectric/triboelectric behavior of BTO/SU-8 photopatternable nanocomposites for highly efficient mechanical energy harvesting, Adv. Electron. Mater **2022**, 2200338 (2022).
[30] H. H. Singh, D. Kumar, and N. Khare, Tuning the performance of ferroelectric polymer-based triboelectric nanogenerator, Appl. Phys. Lett. **119**, 053901 (2021).
[31] F.-R. Fan, Z.-Q. Tian, and Z. L. Wang, Flexible triboelectric generator, Nano Energy **1**, 328 (2012).
[32] L. Dhakar, F. E. H. Tay, and C. Lee, Development of a broadband triboelectric energy harvester with SU-8 micropillars, J. Micro. Syst. **24**, 91 (2014).
[33] A. Yu, Y. Zhu, W. Wang, and J. Zhai, Progress in triboelectric materials: Toward high performance and widespread applications, Adv. Funct. Mater **29**, 1900098 (2019).
[34] K. Zhou, H. Dai, A. Abdelkefi, H. Zhou, and Q. Ni, Impacts of stopper type and material on the broadband characteristics and performance of energy harvesters, AIP Adv. **9**, 035228 (2019).
[35] P. Shaw, Experiments on tribo-electricity. I.—The tribo-electric series, Proc. R. Soc. London. Ser. A, Containing Papers of a Mathematical and Physical Character **94**, 16 (1917).
[36] D. Mallick, A. Amann, and S. Roy, Interplay between electrical and mechanical domains in a high performance nonlinear energy harvester, Smart Mater. Struct. **24**, 122001 (2015).
[37] P. Podder, D. Mallick, A. Amann, and S. Roy, Influence of combined fundamental potentials in a nonlinear vibration energy harvester, Sci. Rep. **6**, 1 (2016).
[38] A. Ibrahim, A. Ramini, and S. Towfighian, Experimental and theoretical investigation of an impact vibration harvester with triboelectric transduction, J. Sound Vibr. **416**, 111 (2018).
[39] See the Supplemental Material at http://link.aps.org/supplemental/10.1103/PRXEnergy.1.033004 for the device process flow, hybrid transduction analysis, concept of the power integral, and numerical simulation, which includes Refs. [40–48].
[40] G. Suo, Y. Yu, Z. Zhang, S. Wang, P. Zhao, J. Li, and X. Wang, Piezoelectric and triboelectric dual effects in mechanical-energy harvesting using $BaTiO_3$/polydimethylsiloxane composite film, ACS Appl. Mater. Interfaces **8**, 34335 (2016).
[41] H. H. Singh and N. Khare, KPFM study of flexible ferroelectric polymer/water interface for understanding the working principle of liquid–solid triboelectric nanogenerator, Adv. Mater. Interfaces **8**, 2100032 (2021).
[42] A. Ahmed, I. Hassan, A. S. Helal, V. Sencadas, A. Radhi, C. K. Jeong, and M. F. El-Kady, Triboelectric nanogenerator versus piezoelectric generator at low frequency (< 4 Hz): A quantitative comparison, Iscience **23**, 101286 (2020).
[43] D. Tantraviwat, M. Ngamyingyoud, W. Sripumkhai, P. Pattamang, G. Rujijanagul, and B. Inceesungvorn, Tuning the dielectric constant and surface engineering of a $BaTiO_3$/Porous PDMS composite film for enhanced triboelectric nanogenerator output performance, ACS Omega **6**, 29765 (2021).
[44] A. Ibrahim, A. Ramini, and S. Towfighian, Triboelectric energy harvester with large bandwidth under harmonic and random excitations, Energy Rep. **6**, 2490 (2020).
[45] C. Liu, (Pearson Education India, Delhi, 2012).
[46] D. Gibus, P. Gasnier, A. Morel, F. Formosa, L. Charleux, S. Boisseau, G. Pillonnet, C. A. Berlitz, A. Quelen, and A. Badel, Strongly coupled piezoelectric cantilevers for broadband vibration energy harvesting, Appl. Energy **277**, 115518 (2020).
[47] C. Chen, R. Zhang, Z. Wang, and W. Cao, Electromechanical coupling coefficient k_{31}^{eff} for arbitrary aspect ratio resonators made of [001] and [011] poled $(1-x)Pb(Mg_{1/3}Nb_{2/3})O_3 - xPbTiO_3$ single crystals, J. Appl. Phys. **105**, 064104 (2009).
[48] W. E. Baker, W. E. Woolam, and D. Young, Air and internal damping of thin cantilever beams, Int. J. Mech. Sci. **9**, 743 (1967).